scientific **data**

Check for updates

Near Pan-Svalbard permafrost cryospheric hazards inventory (*SvalCryo*)

Ionut Cristi Nicu [1] ✉, Lena Rubensdotter[2,3], Hakan Tanyaş [4] & Luigi Lombardo[4]

Cryospheric hazards - in this case, thaw slumps (TS) and thermo-erosion gullies (TEG) - are phenomena typical of permafrost-dominated landscapes. Open datasets informing about their spatial, temporal and size distributions in the Arctic are still uncommon, as opposed to the systematic availability of this information for geomorphic processes in mid- to low- latitudes. To date, only the most populated region of Svalbard was covered with TS and TEG inventories. Here, we extend the respective information to most of the Archipelago, totalling 8491 polygons, out of which 3679 are TSs and 4812 are TEGs. These have been manually mapped from aerial photographs throughout Svalbard across the 14 largest ice-free regions. The *SvalCryo* inventory is highly relevant as the Arctic environment undergoes alarming changes in response to global warming. The idea behind the two inventories is to support the geoscientific community in the quest to evaluate the environmental response to climate change, by creating a baseline for change monitoring, and ultimately to serve as basis for susceptibility, hazard and risk assessment models.

Background & Summary

The cold regions of the Globe are increasingly at risk from the ongoing climate changes. This is leading to rapid environmental dynamics, such as the rapid melting of the polar ice caps, causing sea level rise, changes in ocean currents, and an increase in extreme weather events[1,2]. Permafrost is solid subsurface material that remains continuously at, or below, 0 °C for at least two consecutive years[3]. The active layer (that spans between 0.5–2 m on Svalbard) refers to the layer of soil in areas underlain by permafrost that is subject to annual freezing and thawing, and is where most of the subsurface ecosystem processes occur in the permafrost landscape. The increasing trend of warming temperatures since the 1980s has initiated permanent permafrost degradation at a global scale[4]. The Arctic has warmed four times faster than the rest of the globe since 1979[2]. Irreversible thawing and permanent loss of ice in ice-rich permafrost – known as thermokarst – affects local landforms, ecosystems and, through greenhouse-gas feedback mechanisms, the global climate[5,6]. This is a common problem in the pan-Arctic area[7,8], Antarctica[9,10] and Qinghai-Tibet Plateau – the third Pole[11,12]. As the Arctic warms, methane (the second largest contributor to climate change after carbon dioxide)[13,14], carbon dioxide[15,16], organic carbon[17,18], and nitrogen (nitrous oxide) emissions[19,20] are projected to increase in response to permafrost degradation. Warming and thawing permafrost also has the potential to damage vulnerable and unique cultural-heritage sites in the cold regions[21–24], and pose a serious threat to the sustainable development and resilience of Arctic communities[25], infrastructure[8,11,26,27] and industrial sites[28].

Natural hazards at mid to low latitudes are regularly mapped, allowing scientists to (1) analyse their evolution in time and space, (2) build a shared understanding of the genesis of such processes, and ultimately to (3) support susceptibility, hazard and risk assessment protocols[29] according to the relevant guidelines[30].

This is the case for rainfall-induced landslides[31–33], co-seismic landslides[34], gully erosion[35] and floods[36]. In the present climate context, we advocate for the same consistency to be adopted also for the cold regions of the globe[37]. There has been observed an increasing trend in the publishing of cryospheric hazard data from Arctic regions, but it is still far from the global inventories from mid to low latitudes[38]. Some examples of published datasets are from Yukon, Banks Island, Richardson Mountains-Peel Plateau, and Beaufort Delta Canada[39–42], Alaska, USA[43], Siberia[44–46], Svalbard[47], and Tibetan Plateau[48,49].

[1]High North Department, Norwegian Institute for Cultural Heritage Research (NIKU), Fram Centre, N-9296, Tromsø, Norway. [2]Geohazard and Earth Observation Department, Geological Survey of Norway (NGU), P.O. Box 6315 Torgarden, 7491, Trondheim, Norway. [3]Arctic Geology Department, The University Centre in Svalbard (UNIS), P.O. Box 156, 9171, Longyearbyen, Norway. [4]Faculty of Geo-Information Science and Earth Observation (ITC), University of Twente, PO Box 217, Enschede, AE, 7500, Netherlands. ✉e-mail: ionut.cristi.nicu@niku.no

With the technological advances and the continuous improvement of automated mapping techniques, efforts to produce automated cryospheric inventories for both TS[50–53] and TEG[54] are increasing. However, a consistent accuracy of automatically mapped features requires some degree of adaptation to different data sources (e.g., satellite images) and associated spatial, temporal and spectral characteristics[50,55,56]. This translates into flexible models capable to transfer the mapping procedures from one area to another[53,57].

To assess the available high-resolution (<1 m) aerial images collected by the Norwegian Polar Institute (NPI)[58], we chose to visually interpret and manually map both TSs and TEGs, knowing that this option is more time-consuming but often more accurate compared to automated tools[59–61]. However, due to the scarcity of relevant cryospheric hazard inventories to use as validation datasets, training an AI-model for automated mapping would likely have produced erroneous and unreliable results.

Ideally, an active retrogressive thaw slump (RTS) consists of a headwall, a slump floor and a slump lobe, which are colour-differentiated on aerial or satellite imagery. This feature can continue to expand as the headwall scar retreats, making it more visible in the landscape[45,59]. Conversely, TS are less visible in the landscape and more difficult to map (e.g. Svalbard[47,62]) because their main characteristic is that they are more stable or have a very smooth headwall that has not yet retrograded (or has retrograded at some point in the past but is no longer active). To date, no automated methods have been used to create the TS inventories. This is because the "footprint" they leave in the landscape is usually not large enough or visible enough in most available remote sensing datasets (e.g. Arctic DEM[63]) to be able to train a deep or machine learning system.

A TEG forms when water infiltrates into the frozen soil column warming the surrounding material and causing a loss of cohesion between soil particles. This can occur in or along seasonal frost cracks in the ground, sometimes associated with ice wedge polygons[64,65]. TEGs rely on both soil creep and fluvial transport of particles and can develop both retrogradely upslope and by widening/deepening of the initial incision[66].

The final inventories will be highly relevant for a large suite of scientists from various domains. For biologists, these are useful for habitat assessment, species distribution modelling, conservation planning, and vegetation dynamics[67,68]. For ecologists, this information supports research related to ecological vulnerability assessment, habitat planning and conservation, and ecological resilience[67]. For permafrost scientists, these types of inventories constitute the foundation for susceptibility, hazard, and risk assessment[69], early warning systems, research, and policy-making[70]. Hydrologists may use them to evaluate river discharge[71], whereas polar archaeology selects and prioritizes sites for investigation upon this type of databases, opting for suitable mitigation and conservation planning, adaptation, as well as long-term monitoring[47,62,66,72–74]. For industry, it is critical for risk assessment and planning, infrastructure development, resource extraction, insurance and finance, and emergency preparedness and response[28,75]. For statisticians, complete and high-quality cryospheric hazard inventories are the backbone of any prediction model in the cold regions[47,76–79], with the objective of making inferences concerning triggering mechanisms and future evolution[80]. Ultimately, suitable risk assessment protocols rely on the same information[47,76].

Beyond the modelling aspects, inventories also represent a snapshot of the environmental conditions at a given point in time. As a result, any future update of the same, would inevitably provide information on the changes a given landscape has undergone, quantifying increasing/decreasing trends in cryospheric hazard activity.

All of the above are crucial pieces of a much larger puzzle in which the Artic landscape is threatened by global warming, and the only way the geoscientific community can fully understand the landscape's response is precisely in the form of open data. These considerations apply not only at the level of the Svalbard Archipelago, where the current work has been carried out, but also at the pan-Arctic level. This is also highly relevant in the context of recent studies highlighting a higher temperature sensitivity[81] of TS activity in the Arctic compared to the Third Pole[82]. Therefore, this contribution not only addresses a multidisciplinary need, but also tries to stimulate similar studies elsewhere, as well as follow-up studies in Svalbard.

Methods
The development of TS and TEG inventories for 14 regions of Svalbard followed three main steps: (i) initial mapping of both processes; (ii) validation and quality check of the complete dataset; (iii) processing of geometries, attributes and size characteristics; which were also used before[47] to avoid any bias in the data collection.

Data acquisition. To complete and build a comprehensive inventory of the two cryospheric hazards, we analysed the most recent high-resolution ortophotos (0.5 × 0.5 m), obtained between 2008 and 2011 from the Web Map Services (WMS) provided by the Norwegian Polar Institute[58] in the ETRS_1989_UTM_Zone_33N reference system. There is no subsequent aerial or satellite imagery clear enough to delineate the two landform types exists over the last decade; the Google Earth and ESRI Wayback imagery are of too low resolution, making them unsuitable for detailed mapping. TSs and TEGs were identified based on their morphology, digitised on-screen as polygons at a maximum zoom level of 1:1.000, and then individually checked in the GIS environment. This process was repeated twice, to minimise any bias in the mapping, first by a geomorphologist (first author) and then quality checked and if needed, adjusted by an Arctic geologist (second author) to check quality and make any necessary adjustments. The aim was to produce the inventories of the highest completeness, quality, and representativeness.

Data Records
The cryospheric inventory of the 14 regions (Andreé Land, Dickson Land, James I Land, Nordenskiöld Land, Bünsow Land, Olav V Land, Sabine Land, Nathorst Land, Heer Land, Wedel Jarlsberg Land, Torell Land, Sørkapp Land, Barentsøya and Edgeøya) (Fig. 1) totalises 8491 polygons, out of which 3679 are TS and 4812 are TEG (Table 1). It should be noted the regions were predefined by naming in the Atlas of Svalbard[83,84]. The mapped regions are highly representative for the entire ice-free areas of the Svalbard Archipelago. The inventory is available for download at Zenodo[85], under the name of ***SvalCryo***, in shapefile (.shp) format, that can be imported into any GIS environment. In detail, the inventory is comprised only of vector-polygons. There are two
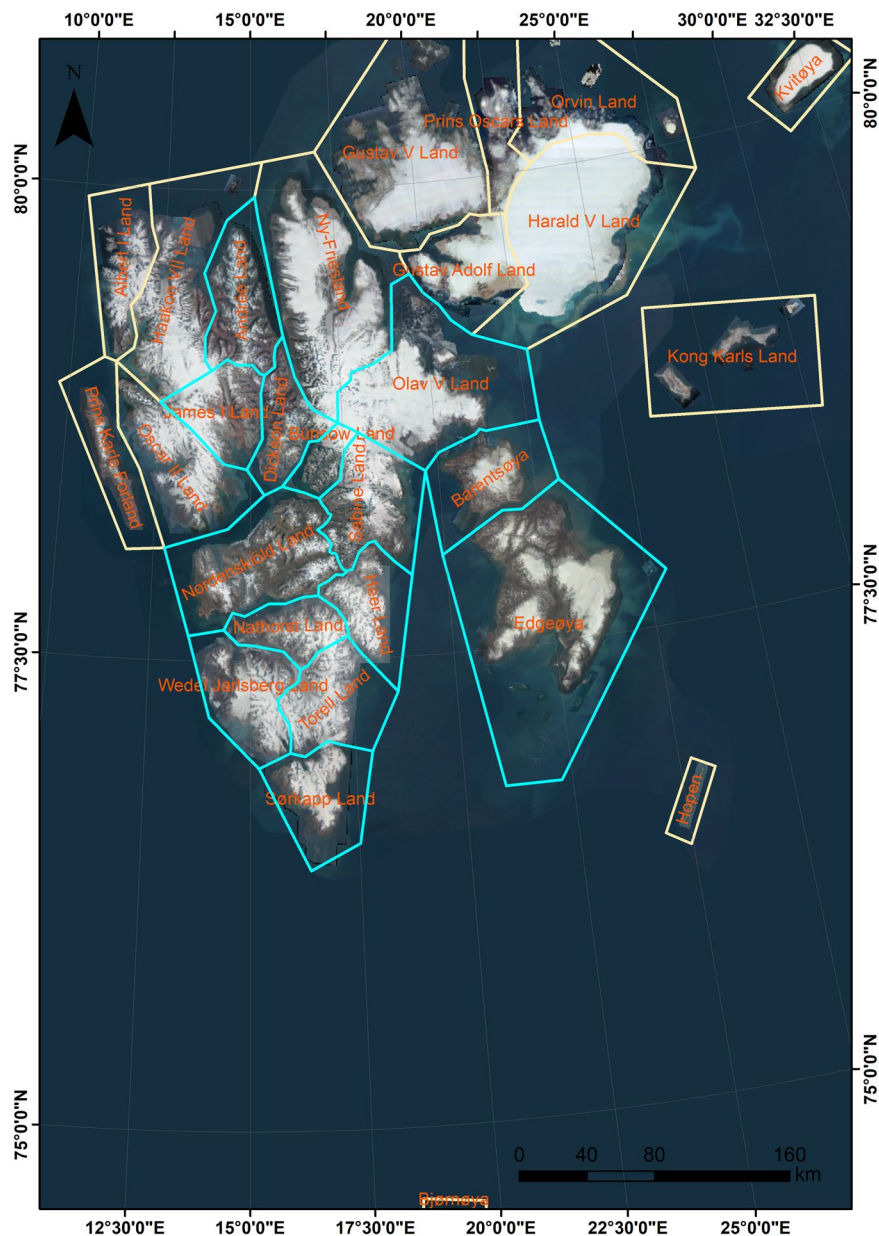
Fig. 1 Location of the 14 regions (light blue polygons) chosen for this study (base map from Norwegian Polar Institute[93]).

main shapefiles, named TS_all and TEG_all, which comprises all the features. Within the attribute tables, there are eight columns, which comprise details about each polygon/feature, as follows:

1. *FID* – ID showing the total number of polygons.
2. *Shape* – Polygon.
3. *ID* – each polygon from each region has associated an ID for both TS and TEG.
4. *Area* – expressed in m^2.
5. *Perimeter* – expressed in m.
6. *Maximum distance* – calculated between two points along the polygon perimeter.
7. *Elongation Index* – calculated as the maximum distance divided by the square root of the area.
8. *Region* – the name of the region that the feature belongs to.

Technical Validation

Compared to the last inventories from Nordenskiöld Land[47], which contained 562 TS and 908 TEG, the **SvalCryo** inventory presented here adds a significant amount of data for the Svalbard Archipelago, reaching a total of 3679 TS and 4812 TEG. Since the data have been produced and validated by two different scientists with different backgrounds, it can be said that they are of high completeness, quality, and representativeness in local,

Region name	Thaw slumps (TS)	Thermo-erosion gullies (TEG)
Andreé Land	280	378
Dickson Land	410	581
James I Land	212	154
Nordenskiöld Land	562	908
Bünsow Land	80	47
Olav V Land	51	370
Sabine Land	91	417
Nathorst Land	378	276
Heer Land	116	635
Wedel Jarlsberg Land	301	281
Torell Land	0	0
Sørkapp Land	183	175
Barentsøya	235	206
Edgeøya	780	384
TOTAL	**3679**	**4812**

Table 1. Details (numbers) of the two cryospheric hazards for each region.
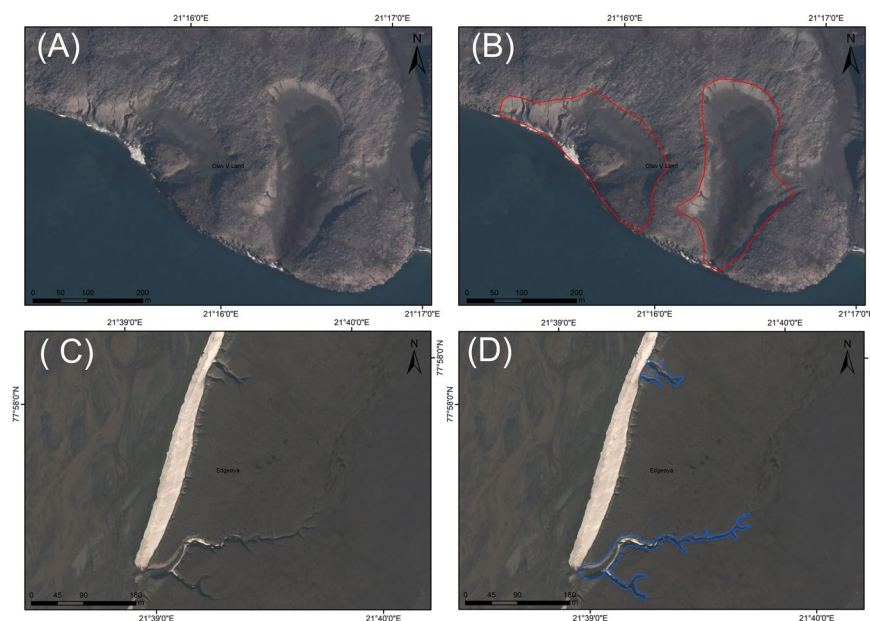
Fig. 2 Detail over some of the mapped features (**A**) Identification of two TS located in Olav V Land, before digitization. (**B**) The same two TS after digitization (**C**) Identification of three TEG on Edgeøya, before digitization. (**D**) The same three TEG after digitization. There are even smaller potential TEGs visible along the snow field in this image, not mapped due to scale compared with decided zoom level at digitising.

regional and pan-Arctic contexts and scales. To provide a better glimpse into the mapped TS and TEG features, we highlight some of them Fig. 2.

Completeness and quality of records. The consistency and completeness of an inventory is highly dependent on the quality of the optical imagery as well as the scale at which an area of interest extends and is surveyed[86]. Any automated techniques used to map TS and TEG from different cartographic materials and aerial photographs require a robust and high quality dataset, usually built up from manual interpretations, to ensure that any AI protocol adequately learns and reproduces relevant features. Some representative features have also been identified and observed in the field (examples in Fig. 2) to verify the remote sensing results. Our inventory includes features, both TS and TEG, that can be identified on screen up to a maximum zoom level of 1:1000. This approach allows unambiguous identification, in balance with the quality of the remote sensing data, while ensuring a consistent spatial accuracy of the final datasets. We did not map any features that we judged ambiguous, or formed by overlapping processes.
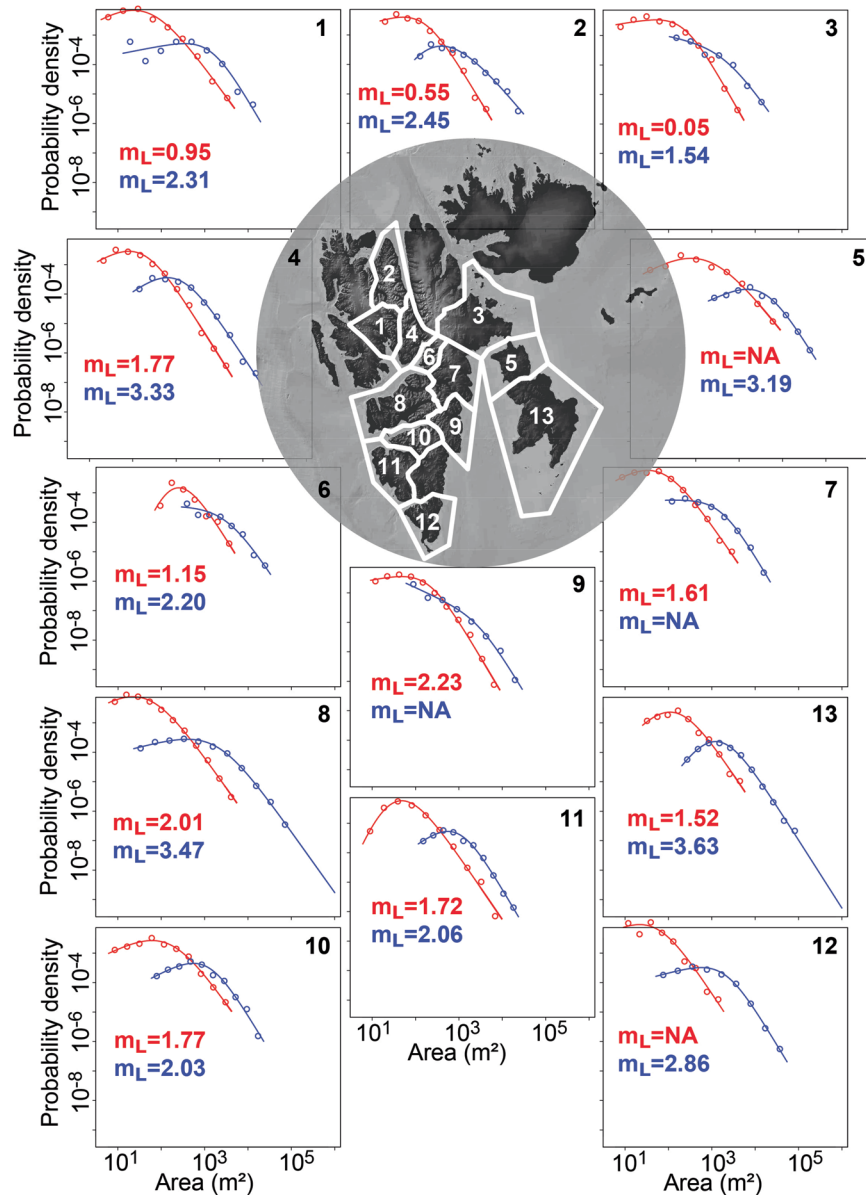
Fig. 3 Plotted FAD for the 13 regions covered by the inventory. In blue we report TS data whereas in red correspond to TEG. A few regions are shown with m_L values labelled as NA. This is due to the underlying calculation of the FAD, which involves a fitting a statistical model whose results are dependent on the data size. When the population is too small, the results of the statistical procedure tend to become unstable, and the results are not reported.

Activities to validate the completeness and quality of the inventory were carried out across the entire dataset. Through this approach, the ***SvalCryo*** inventory is thoroughly assessed and improved, ensuring a robust and reliable dataset for further analysis and decision-making in the context of climate change and Arctic landscape management. The completeness of an inventory has an impact on the Frequency-Area Distribution (FAD). The FAD of a TS or TEG event quantifies the number of TS and TEGs occurring at different sizes[86,87]. In Fig. 3, we have plotted the FAD for both processes (TS in red and TEG in blue) for each region individually. Torell Land is not included in the analysis as there were no TS or TEG present.

In addition, we also report the event magnitude (m_L), an index that has been scientifically introduced for landslides[88] to give a value of the intensity of the present population. In this case, this value can be interpreted as the proportional intensity (number and size) of the TS and TEG as the value increases. This value is obtained by a best-fit line through the TS and TEG respective FADs. In a few regions, we have avoided reporting for one or the other parameter (TS or TEG). The reason for this choice is the limited TS and TEG population in these regions, which inevitably affects the m_L estimates. In general, when looking at the respective m_L values for TS and TEG (Fig. 3),the former (in blue) is generally associated with higher values, compared to the latter (in red).
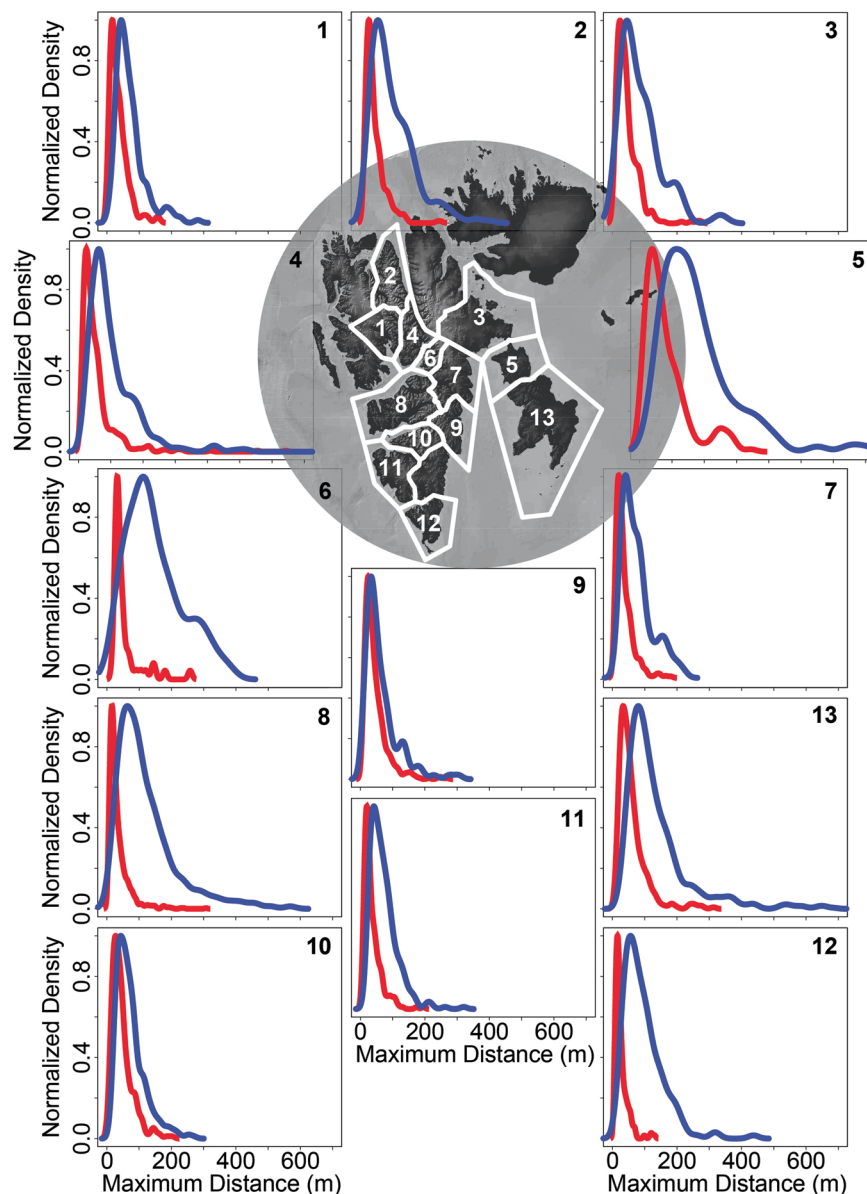
Fig. 4 Distribution of *Maximum Distance* across the 13 regions. TS are shown in blue, TEG are reported in red.

This can be intuitively justified by the genetically much larger planimetric area of a standard TS as compared to a TEG, since a TS is by nature a laterally extending surface of thawed sediment which are displaced laterally, whereas a TEG is formed along a thin fluvial centreline by mainly grain-by-grain displacement and subsequent transport. In terms of what the FAD parameter conveys at the scale of the whole Archipelago, it shows that TS are much larger in the region 13 (Edgeøya), compared to the others, while TEGs are much more developed in region 8 (Nordenskiöld Land) as compared to the others.

We do not go deeper into the mechanism in this paper, but one could speculate on the respective influence of geology and local climatic parameters in influencing the different processes. TS are naturally very sensitive to the internal ice content of the permafrost. This, in turn, is related to the porosity and morphology/connectivity of the pore spaces that form the conduits for the movement of soil-water in the deposits, and hence the potential rate of water movement to freezing fronts[89]. Pore spaces and pore morphology are in turn closely related to the grain size and grain size distribution in the soil, which is physically related to the bedrock provenance (minerology). It is therefore reasonable to assume that variations in TS FAD are, at least in part, related to parent bedrock types in different areas of Svalbard, as well as to thaw season temperatures. TEGs are logically related to similar mechanisms concerning soil ice-content, but their areal development and growth rate are also closely related to the removal of solid grains by surface water flow to allow further exposure and degradation of soil-ice in the gully sides. Surface water flow is related to both the regional precipitation pattern around Svalbard and to the topography, as much of the winter precipitation falls irregularly across the landscape as wind-driven snow. The variation in TEG FAD may therefore be less easily deciphered as being related to geology and more dependent on other, independent factors.
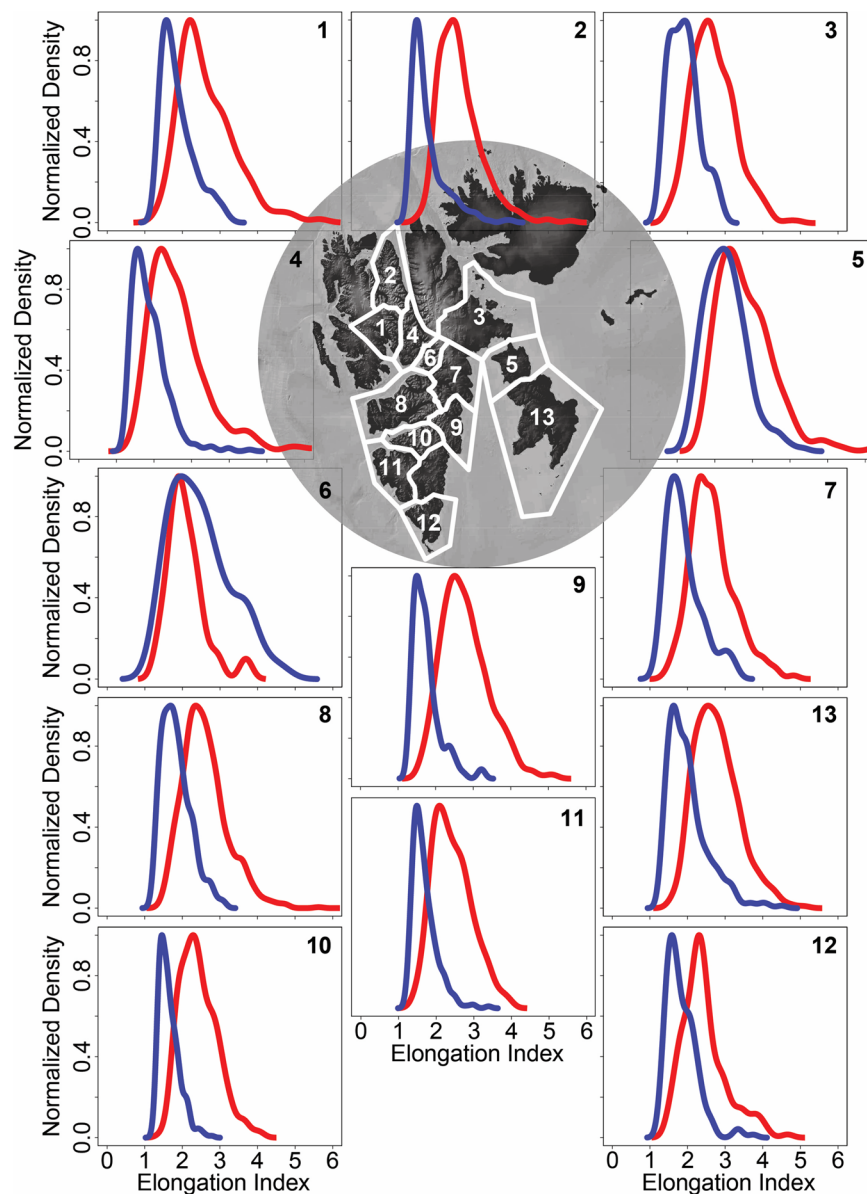
Fig. 5 *Elongation Index* for the 13 regions.

Overall representativeness and coverage of records. The inventory covers a very large part of the ice-free area of the Svalbard Archipelago. This means areas where both processes can initiate and further develop. In the current climate context and for further understanding of the triggering mechanisms and development patterns of both TS and TEG, this is undoubtedly a step forward, and in the context of TS and TEG risk assessment and multi-hazard susceptibility, a high quality, representative inventory across the majority of the Svalbard Archipelago is a fundamental achievement. This is also of great importance in the context of Svalbard's geology, which is known to be represented by rock formations from virtually all geological eras[90]. Due to its structure, the *SvalCryo* inventory offers users the possibility to carry out research and different types of analysis from local to regional scales in an easier and more consistent way. Examples include, but are not limited to: analysis of the controlling environmental factors (which can be derived from the ArcticDEM database[63]) of the two processes, their size parameters, analysis of the possible impacts of TS and TEG on Arctic infrastructure and cultural heritage sites, their distribution in selected areas, such as geologically homogeneous areas or in relation to administrative boundaries. Therefore, they were grouped according to the administrative regions of Svalbard. This is because each region has its specific climatic factors (precipitation, temperature)[91,92] that influence both processes. Below are some examples where we have plotted the parameters *Maximum Distance* (Fig. 4) and *Elongation Index* (Fig. 5) to give an example of what can be achieved with further processing.

The *Maximum Distance* is essentially the longest segment that can be drawn between any pair of points distributed along the TS or TEG polygons. It is clear from Fig. 4 is that the TEG are generally underdeveloped, with their longest expression of approximately 400 m being reached in region 5 (Barentsøya). Another general indication of TEG underdevelopment can be seen in the heavy tailed and positively skewed distributions typical
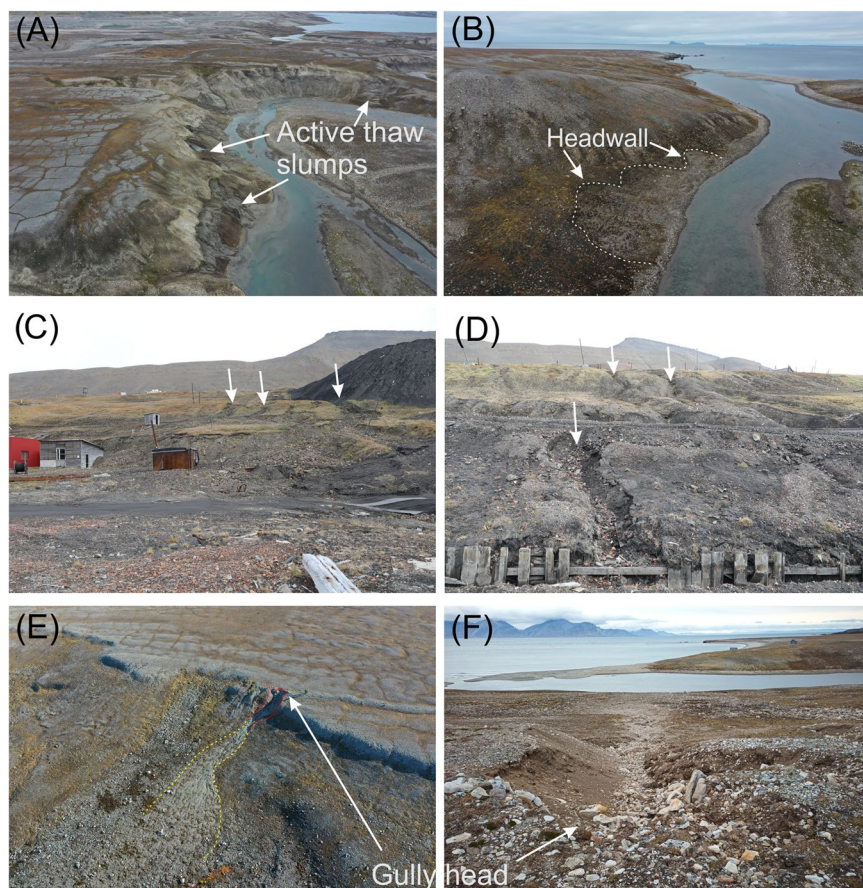
Fig. 6 Ground truthing of some mapped features. (**A**) UAV photo of active thaw slumps on the right side of Linnéelva river, close to Russekeila in 2020. (**B**) Freshly initiated thaw slump on the left side of Linnéelva river in 2020. (**C, D**) Arrows indicate active thermo-erosion gullies in the proximity of Barentsburg in 2021. (**E**) UAV photo of a freshly initiated thermo-erosion gully on the left side of Linnéelva river (in red is highlighted the gully head, in yellow is highlighted the deposition area) in 2020. (**F**) The same thermo-erosion gully in 2022.

of each of the regions considered, with the bulk of the distribution centred within a few tens of meters. In terms of TS maximum distance distributions, these are also heavily tailed and positively skewed, but the range of the bulk is much wider. Interestingly, the TEGs can be quite long, with a maximum overall distance of about 700 m being reached in three regions (4 – Dickson Land, 5 – Barentsøya, and 13 – Edgeøya). The long TEGs in some regions may be the result of one or several combined factors, such as the geographical extent of sedimentolog-ically homogeneous deposits, e.g. large coastal plains of isostatically uplifted fine-grained marine sediments, together with favourable precipitation and climatic conditions for a long thawing season with regular precipita-tion, providing the excess water needed for fluvial sediment transport out of the gullies. The opposite may be the explanation for regions with generally smaller TEGs; laterally confined favourable deposits in the valley bottom, and/or a higher degree of internally varying sediment types, e.g. with spatially varying grain-size compositions from the central valleys towards the till- or talus-covered slopes. High spatial variability of unconsolidated sed-iment types would hinder TEG development, even if climatic factors are favourable.

Another parameter we have chosen to present is the *Elongation Index* (Fig. 5). This metric is obtained by combining the two metrics presented above (planimetric area and maximum distance). The formula links the two parameters by dividing the *Maximum Distance* by the square root of the planimetric area. The interpretation is therefore that, from a physical point of view, the *Elongation Index* is unitless, and its interpretation assumes that larger values would indicate polygons whose length is much greater than their transformed planimetric extent. In other words, values around one correspond to round to very round polygons, while values progres-sively larger indicate an elongation along a single axis. For TS, this value is less obvious to interpret, as the elongation index is not related to any lateral or retrogressive development of the TS. This information requires a more detailed study of each feature, which we did not focus on the first inventory. However, as we know from our mapping experience that the TS occurrences far outnumber the RTS in the Svalbard inventory, we may the-orise that the more elongated TS are related to development along lateral erosional scarps in the terrain – usually associated with incising glaciofluvial rives. Thus, this index may capture a combination of favourable conditions for TS (discussed in the section above) with the presence of incised rivers in different regions. For TEG, the *Elongation Index* is logically most related to the same factors as the maximum distance index, since the TEG

process itself works narrowly backwards into low angle deposits with homogeneous sediment properties, we expect favourable conditions in terms of both size and elongation to be the same.

***SvalCryo* inventory limitations.** Some technical limitations must be mentioned due to the approach used to develop the *SvalCryo* inventory. First of all, the main limitation of the inventory is its temporal coverage. The polygons represent the reality on the ground as it was in 2009–2011. From another point of view, this is a strength for future change analysis. Considering the large area of the Archipelago, manual mapping at 1:1000 scale was quite a time-consuming process. However, we did our best to overcome the potential negative effects on homogeneity of quality, taking into account the double validation process by two independent scientists. The limitation of ground truthing should be mentioned. There were limited opportunities to be in the field during the summer season to validate our inventory, due to both scheduling and Arctic field challenges and high costs. However, as shown in Fig. 6, some limited ground truthing was carried out as well as drawing on previous experience from other Svalbard mapping projects by operator from NGU/UNIS. Another limitation is that TS and TEG were not mapped beyond the 1:1000 zoom level.

Usage Notes

The *SvalCryo* inventory is available in the repository[85]. It is intended to be open and available to all permafrost researchers, users and authorities. The entire digitisation process has been carried out in ArcGIS v10.6.1, but all items have been produced in a format that can be imported into any GIS environment. We did our best to map all the visible features representing a TS and a TEG at a 1:1000 zoom level. There is therefore a possibility that smaller features visible beyond this zoom level may not be mapped. Future versions of the inventory will be extended to other ice-free areas, with the aim of covering the entire Archipelago. It is also hoped that more recent ortophotos will become available, allowing the repeated mapping of both processes in order to analyse their spatio-temporal evolution.

Code availability

No customized code was produced to create or analyse this dataset because software that works in a GIS environment is required to open and further process the *SvalCryo* inventory. Specifically, we used ArcGIS v10.6.1 software to create the dataset, but the *SvalCryo* inventory can be opened with any GIS software (open-sourced or licensed).

References

1. Yu, L., Zhong, S. & Sun, B. Trends in the occurrence of pan-Arctic warm extremes in the past four decades. *International Journal of Climatology* **41**, 4460–4477, https://doi.org/10.1002/joc.7069 (2021).
2. Rantanen, M. *et al*. The Arctic has warmed nearly four times faster than the globe since 1979. *Communications Earth & Environment* **3**, 168, https://doi.org/10.1038/s43247-022-00498-3 (2022).
3. Liao, C. & Zhuang, Q. Quantifying the Role of Permafrost Distribution in Groundwater and Surface Water Interactions Using a Three-Dimensional Hydrological Model. *Arctic, Antarctic, and Alpine Research* **49**, 81–100, https://doi.org/10.1657/aaar0016-022 (2018).
4. Biskaborn, B. K. *et al*. Permafrost is warming at a global scale. *Nature Communications* **10**, 264, https://doi.org/10.1038/s41467-018-08240-4 (2019).
5. Wassmann, P. *et al*. Towards a unifying pan-arctic perspective: A conceptual modelling toolkit. *Progress in Oceanography* **189**, 102455, https://doi.org/10.1016/j.pocean.2020.102455 (2020).
6. Jin, H.-J., Yang, D., Makarieva, O. & Tang, L. Changes in permafrost and snow cover in the Boreal and Arctic zones (BAZs) and their impacts. *Advances in Climate Change Research* **14**, 157–163, https://doi.org/10.1016/j.accre.2023.04.002 (2023).
7. Ran, Y. *et al*. New high-resolution estimates of the permafrost thermal state and hydrothermal conditions over the Northern Hemisphere. *Earth System Science Data* **14**, 865–884, https://doi.org/10.5194/essd-14-865-2022 (2022).
8. Karjalainen, O. *et al*. Circumpolar permafrost maps and geohazard indices for near-future infrastructure risk assessments. *Scientific Data* **6**, 190037, https://doi.org/10.1038/sdata.2019.37 (2019).
9. Oliva, M. & Ruiz-Fernández, J. Coupling patterns between para-glacial and permafrost degradation responses in Antarctica. *Earth Surface Processes and Landforms* **40**, 1227–1238, https://doi.org/10.1002/esp.3716 (2015).
10. Lacelle, D., Fisher, D. A., Verret, M. & Pollard, W. Improved prediction of the vertical distribution of ground ice in Arctic-Antarctic permafrost sediments. *Communications Earth & Environment* **3**, 31, https://doi.org/10.1038/s43247-022-00367-z (2022).
11. Ran, Y. *et al*. Permafrost degradation increases risk and large future costs of infrastructure on the Third Pole. *Communications Earth & Environment* **3**, 238, https://doi.org/10.1038/s43247-022-00568-6 (2022).
12. Huang, S. *et al*. Changes in near-surface permafrost temperature and active layer thickness in Northeast China in 1961–2020 based on GIPL model. *Cold Regions Science and Technology* **206**, 103709, https://doi.org/10.1016/j.coldregions.2022.103709 (2022).
13. Rößger, N., Sachs, T., Wille, C., Boike, J. & Kutzbach, L. Seasonal increase of methane emissions linked to warming in Siberian tundra. *Nature Climate Change* **12**, 1031–1036, https://doi.org/10.1038/s41558-022-01512-4 (2022).
14. Knoblauch, C. *et al*. Carbon Dioxide and Methane Release Following Abrupt Thaw of Pleistocene Permafrost Deposits in Arctic Siberia. *Journal of Geophysical Research: Biogeosciences* **126**, e2021JG006543, https://doi.org/10.1029/2021jg006543 (2021).
15. Miner, K. R. *et al*. Permafrost carbon emissions in a changing Arctic. *Nature Reviews Earth & Environment* **3**, 55–67, https://doi.org/10.1038/s43017-021-00230-3 (2022).
16. Rodenhizer, H. *et al*. Abrupt permafrost thaw accelerates carbon dioxide and methane release at a tussock tundra site. *Arctic, Antarctic, and Alpine Research* **54**, 443–464, https://doi.org/10.1080/15230430.2022.2118639 (2022).
17. Ramage, J. L., Irrgang, A. M., Morgenstern, A. & Lantuit, H. Increasing coastal slump activity impacts the release of sediment and organic carbon into the Arctic Ocean. *Biogeosciences* **15**, 1483–1495, https://doi.org/10.5194/bg-15-1483-2018 (2018).
18. Bernhard, P., Zwieback, S. & Hajnsek, I. Accelerated mobilization of organic carbon from retrogressive thaw slumps on the northern Taymyr Peninsula. *The Cryosphere* **16**, 2819–2835, https://doi.org/10.5194/tc-16-2819-2022 (2022).
19. Marushchak, M. E. *et al*. Thawing Yedoma permafrost is a neglected nitrous oxide source. *Nature Communications* **12**, 7107, https://doi.org/10.1038/s41467-021-27386-2 (2021).

20. Strauss, J. *et al.* A globally relevant stock of soil nitrogen in the Yedoma permafrost domain. *Nature Communications* **13**, 6074, https://doi.org/10.1038/s41467-022-33794-9 (2022).

21. Hollesen, J. *et al.* Climate change and the deteriorating archaeological and environmental archives of the Arctic. *Antiquity* **92**, 573–586, https://doi.org/10.15184/aqy.2018.8 (2018).

22. Nicu, I. C. & Fatorić, S. Climate change impacts on immovable cultural heritage in polar regions: A systematic bibliometric review. *WIREs Climate Change* **14**, e822, https://doi.org/10.1002/wcc.822 (2023).

23. Gaiser, R. F., Robles, C. A., Skronski, N., Kobashigawa, J. M. & Carmaran, C. C. Historical Heritage in Antarctica, The Casa Moneta Museum: A First Approach to the Characterization of Xylophagous Fungi and Their Potential Role in Wood Damage. *International Journal of Conservation Science* **14**, 1391–1404, https://doi.org/10.36868/IJCS.2023.04.09 (2023).

24. Hollesen, J., Jepsen, M. S., Stendel, M. & Harmsen, H. Assessing the consequences of recent climate change on World Heritage sites in South Greenland. *Sci Rep* **14**, 9732, https://doi.org/10.1038/s41598-024-60397-9 (2024).

25. Alessa, L. *et al.* Toward a Permafrost Vulnerability Index for Critical Infrastructure, Community Resilience and National Security. *Geographies* **3**, 522–542, https://doi.org/10.3390/geographies3030027 (2023).

26. Hjort, J. *et al.* Impacts of permafrost degradation on infrastructure. *Nature Reviews Earth & Environment* **3**, 24–38, https://doi.org/10.1038/s43017-021-00247-8 (2022).

27. Scheer, J., Tomaškovičová, S. & Ingeman-Nielsen, T. Thaw settlement susceptibility mapping for roads on permafrost - Towards climate-resilient and cost-efficient infrastructure in the Arctic. *Cold Regions Science and Technology* **220**, https://doi.org/10.1016/j.coldregions.2024.104136 (2024).

28. Langer, M. *et al.* Thawing permafrost poses environmental threat to thousands of sites with legacy industrial contamination. *Nature Communications* **14**, 1721, https://doi.org/10.1038/s41467-023-37276-4 (2023).

29. Hervás, J. & Bobrowsky, P. in *Landslides – Disaster Risk Reduction* (eds K. Sassa & P. Canuti) 321-349 (Springer, 2009).

30. Fell, R. *et al.* Guidelines for landslide susceptibility, hazard and risk zoning for land use planning. *Engineering Geology* **102**, 85–98, https://doi.org/10.1016/j.enggeo.2008.03.022 (2008).

31. Fusco, F. *et al.* A revised landslide inventory of the Campania region (Italy). *Scientific Data* **10**, 355, https://doi.org/10.1038/s41597-023-02155-6 (2023).

32. Emberson, R., Kirschbaum, D. B., Amatya, P., Tanyas, H. & Marc, O. Insights from the topographic characteristics of a large global catalog of rainfall-induced landslide event inventories. *Natural Hazards and Earth System Sciences* **22**, 1129–1149, https://doi.org/10.5194/nhess-22-1129-2022 (2022).

33. Santangelo, M. *et al.* Inventory of landslides triggered by an extreme rainfall event in Marche-Umbria, Italy, on 15 September 2022. *Sci Data* **10**, 427, https://doi.org/10.1038/s41597-023-02336-3 (2023).

34. Tanyaş, H. *et al.* Presentation and Analysis of a Worldwide Database of Earthquake-Induced Landslide Inventories. *Journal of Geophysical Research: Earth Surface* **122**, 1991–2015, https://doi.org/10.1002/2017jf004236 (2017).

35. Han, J., Guzman, J. A. & Chu, M. L. Gully erosion susceptibility considering spatiotemporal environmental variables: Midwest U.S. region. *Journal of Hydrology: Regional Studies* **43**, 101196, https://doi.org/10.1016/j.ejrh.2022.101196 (2022).

36. Adhikari, P. *et al.* A digitized global flood inventory (1998–2008): compilation and preliminary results. *Natural Hazards* **55**, 405–422, https://doi.org/10.1007/s11069-010-9537-2 (2010).

37. Yao, T. *et al.* Third Pole Environment (TPE). *Environmental Development* **3**, 52–64, https://doi.org/10.1016/j.envdev.2012.04.002 (2012).

38. Guzzetti, F. *et al.* Landslide inventory maps: New tools for an old problem. *Earth-Science Reviews* **112**, 42–66, https://doi.org/10.1016/j.earscirev.2012.02.001 (2012).

39. Ramage, J. L. *et al.* Terrain controls on the occurrence of coastal retrogressive thaw slumps along the Yukon Coast, Canada. *Journal of Geophysical Research: Earth Surface* **122**, 1619–1634, https://doi.org/10.1002/2017jf004231 (2017).

40. Lewkowicz, A. G. & Way, R. G. Extremes of summer climate trigger thousands of thermokarst landslides in a High Arctic environment. *Nature Communications* **10**, 1329, https://doi.org/10.1038/s41467-019-09314-7 (2019).

41. van der Sluijs, J., Kokelj, S. V. & Tunnicliffe, J. F. Allometric scaling of retrogressive thaw slumps. *The Cryosphere* **17**, 4511–4533, https://doi.org/10.5194/tc-17-4511-2023 (2023).

42. Lacelle, D., Brooker, A., Fraser, R. H. & Kokelj, S. V. Distribution and growth of thaw slumps in the Richardson Mountains–Peel Plateau region, northwestern Canada. *Geomorphology* **235**, 40–51, https://doi.org/10.1016/j.geomorph.2015.01.024 (2015).

43. Swanson, D. K. Permafrost thaw-related slope failures in Alaska's Arctic National Parks, c. 1980–2019. *Permafrost and Periglacial Processes* **32**, 392–406, https://doi.org/10.1002/ppp.2098 (2021).

44. Ardelean, F. *et al.* Assessment of Spatio-Temporal Landscape Changes from VHR Images in Three Different Permafrost Areas in the Western Russian Arctic. *Remote Sensing* **12**, 3999, https://doi.org/10.3390/rs12233999 (2020).

45. Runge, A., Nitze, I. & Grosse, G. Remote sensing annual dynamics of rapid permafrost thaw disturbances with LandTrendr. *Remote Sensing of Environment* **268**, 112752, https://doi.org/10.1016/j.rse.2021.112752 (2022).

46. Séjourné, A. *et al.* Evolution of the banks of thermokarst lakes in Central Yakutia (Central Siberia) due to retrogressive thaw slump activity controlled by insolation. *Geomorphology* **241**, 31–40, https://doi.org/10.1016/j.geomorph.2015.03.033 (2015).

47. Nicu, I. C., Elia, L., Rubensdotter, L., Tanyas, H. & Lombardo, L. Multi-hazard susceptibility mapping of cryospheric hazards in a high-Arctic environment: Svalbard Archipelago. *Earth System Science Data* **15**, 447–464, https://doi.org/10.5194/essd-15-447-2023 (2023).

48. Mu, C. *et al.* Acceleration of thaw slump during 1997–2017 in the Qilian Mountains of the northern Qinghai-Tibetan plateau. *Landslides* **17**, 1051–1062, https://doi.org/10.1007/s10346-020-01344-3 (2020).

49. Xia, Z. *et al.* Retrogressive thaw slumps along the Qinghai–Tibet Engineering Corridor: a comprehensive inventory and their distribution characteristics. *Earth System Science Data* **14**, 3875–3887, https://doi.org/10.5194/essd-14-3875-2022 (2022).

50. Huang, L. *et al.* Accuracy, Efficiency, and Transferability of a Deep Learning Model for Mapping Retrogressive Thaw Slumps across the Canadian Arctic. *Remote Sensing* **14**, 2747, https://doi.org/10.3390/rs14122747 (2022).

51. Huang, L., Luo, J., Lin, Z., Niu, F. & Liu, L. Using deep learning to map retrogressive thaw slumps in the Beiluhe region (Tibetan Plateau) from CubeSat images. *Remote Sensing of Environment* **237**, 111534, https://doi.org/10.1016/j.rse.2019.111534 (2020).

52. Nitze, I., Heidler, K., Barth, S. & Grosse, G. Developing and Testing a Deep Learning Approach for Mapping Retrogressive Thaw Slumps. *Remote Sensing* **13**, 4294, https://doi.org/10.3390/rs13214294 (2021).

53. Lin, Y. & Jensen Knudby, A. A transfer learning approach for automatic mapping of retrogressive thaw slumps (RTSs) in the western Canadian Arctic. *International Journal of Remote Sensing* **44**, 2039–2063, https://doi.org/10.1080/01431161.2023.2195571 (2023).

54. Huang, L., Liu, L., Jiang, L. & Zhang, T. Automatic Mapping of Thermokarst Landforms from Remote Sensing Images Using Deep Learning: A Case Study in the Northeastern Tibetan Plateau. *Remote Sensing* **10**, 2067, https://doi.org/10.3390/rs10122067 (2018).

55. Yang, Y. *et al.* Mapping retrogressive thaw slumps using deep neural networks. *Remote Sensing of Environment* **288**, https://doi.org/10.1016/j.rse.2023.113495 (2023).

56. Huang, L. *et al.* Identifying active retrogressive thaw slumps from ArcticDEM. *ISPRS Journal of Photogrammetry and Remote Sensing* **205**, 301–316, https://doi.org/10.1016/j.isprsjprs.2023.10.008 (2023).

57. Wang, Z. & Brenning, A. Unsupervised active–transfer learning for automated landslide mapping. *Computers & Geosciences* **181**, https://doi.org/10.1016/j.cageo.2023.105457 (2023).

58. Institute, N. P. *Svalbard Orthophoto*, https://geodata.npolar.no/arcgis/rest/services/Basisdata/NP_Ortofoto_Svalbard_WMTS_25833/MapServer/WMTS/1.0.0/WMTSCapabilities.xml.

59. Luo, J. *et al.* Inventory and Frequency of Retrogressive Thaw Slumps in Permafrost Region of the Qinghai–Tibet Plateau. *Geophysical Research Letters* **49**, e2022GL099829, https://doi.org/10.1029/2022gl099829 (2022).

60. Kokelj, S. V. *et al.* The Northwest Territories Thermokarst Mapping Collective: A northern-driven mapping collaborative toward understanding the effects of permafrost thaw. *Arctic Science* **9**, 886–918, https://doi.org/10.1139/as-2023-0009 (2023).

61. Peng, X. *et al.* The first hillslope thermokarst inventory for the permafrost region of the Qilian Mountains. *Earth System Science Data* **16**, 2033–2045, https://doi.org/10.5194/essd-16-2033-2024 (2024).

62. Nicu, I. C., Lombardo, L. & Rubensdotter, L. Preliminary assessment of thaw slump hazard to Arctic cultural heritage in Nordenskiöld Land, Svalbard. *Landslides* **18**, 2935–2947, https://doi.org/10.1007/s10346-021-01684-8 (2021).

63. Porter, C. e. a. (ed Harvard Dataverse) (OpenTopography, 2023).

64. Godin, E., Fortier, D. & Coulombe, S. Effects of thermo-erosion gullying on hydrologic flow networks discharge and soil loss. *Environmental Research Letters* **9**, 105010, https://doi.org/10.1088/1748-9326/9/10/105010 (2014).

65. Godin, E., Osinski, G. R., Harrison, T. N., Pontefract, A. & Zanetti, M. Geomorphology of Gullies at Thomas Lee Inlet, Devon Island, Canadian High Arctic. *Permafrost and Periglacial Processes* **30**, 19–34, https://doi.org/10.1002/ppp.1992 (2019).

66. Nicu, I. C., Tanyas, H., Rubensdotter, L. & Lombardo, L. A glimpse into the northernmost thermo-erosion gullies in Svalbard archipelago and their implications for Arctic cultural heritage. *Catena* **212**, 106105, https://doi.org/10.1016/j.catena.2022.106105 (2022).

67. Verdonen, M., Berner, L. T., Forbes, B. C. & Kumpula, T. Periglacial vegetation dynamics in Arctic Russia: decadal analysis of tundra regeneration on landslides with time series satellite imagery. *Environmental Research Letters* **15**, 105020, https://doi.org/10.1088/1748-9326/abb500 (2020).

68. Cassidy, A. E., Christen, A. & Henry, G. H. R. Impacts of active retrogressive thaw slumps on vegetation, soil, and net ecosystem exchange of carbon dioxide in the Canadian High Arctic. *Arctic Science* **3**, 179–202, https://doi.org/10.1139/as-2016-0034 (2017).

69. Kizyakov, A. I. *et al.* Landforms and degradation pattern of the Batagay thaw slump, Northeastern Siberia. *Geomorphology* **420**, 108501, https://doi.org/10.1016/j.geomorph.2022.108501 (2023).

70. Zhang, H., Wang, H., Zhang, J., Luo, J. & Yin, G. Automatic Identification of Thaw Slumps Based on Neural Network Methods and Thaw Slumping Susceptibility. *International Journal of Disaster Risk Science* **14**, 539–548, https://doi.org/10.1007/s13753-023-00504-y (2023).

71. Owczarek, P., Opala-Owczarek, M., Boudreau, S., Lajeunesse, P. & Stachnik, L. Re-activation of landslide in sub-Arctic areas due to extreme rainfall and discharge events (the mouth of the Great Whale River, Nunavik, Canada). *Science of the Total Environment* **744**, 140991, https://doi.org/10.1016/j.scitotenv.2020.140991 (2020).

72. Tavakoli, S., Nicu, I. C., Frauenfelder, R. & Gilbert, G. First geophysical investigations to study a fragile Pomor cultural heritage site at Russekeila – Kapp Linné, Svalbard. *Journal of Cultural Heritage* **63**, 187–193, https://doi.org/10.1016/j.culher.2023.08.005 (2023).

73. Aktürk, G. A systematic overview of the barriers to building climate adaptation of cultural and natural heritage sites in polar regions. *Environmental Science & Policy* **136**, 19–32, https://doi.org/10.1016/j.envsci.2022.05.016 (2022).

74. Nicu, I. C., Granberg, M. & Undall, E. Short overview on international historic climate adaptation of built heritage to natural hazards: lessons for Norway. *International Journal of Conservation Science* **13**, 441–456 (2022).

75. Korsgaard, N. J. *et al.* Evidence of Middle Holocene landslide-generated tsunamis recorded in lake sediments from Saqqaq, West Greenland. *Natural Hazards and Earth System Sciences* **24**, 757–772, https://doi.org/10.5194/nhess-24-757-2024 (2024).

76. Elia, L., Castellaro, S., Dahal, A. & Lombardo, L. Assessing multi-hazard susceptibility to cryospheric hazards: Lesson learnt from an Alaskan example. *Science of the Total Environment*, 165289, https://doi.org/10.1016/j.scitotenv.2023.165289 (2023).

77. Yin, G. *et al.* High-resolution assessment of retrogressive thaw slump susceptibility in the Qinghai-Tibet Engineering Corridor. *Research in Cold and Arid Regions* https://doi.org/10.1016/j.rcar.2023.11.006 (2023).

78. Luo, J. *et al.* Machine learning-based predictions of current and future susceptibility to retrogressive thaw slumps across the Northern Hemisphere. *Advances in Climate Change Research* https://doi.org/10.1016/j.accre.2024.03.001 (2024).

79. Makopoulou, E. *et al.* Retrogressive thaw slump susceptibility in the northern hemisphere permafrost region. *Earth Surface Processes and Landforms*, https://doi.org/10.1002/esp.5890 (2024).

80. Li, Y. *et al.* Advances in retrogressive thaw slump research in permafrost regions. *Permafrost and Periglacial Processes* **35**, 125–142, https://doi.org/10.1002/ppp.2218 (2024).

81. Dahlke, S. *et al.* The observed recent surface air temperature development across Svalbard and concurring footprints in local sea ice cover. *International Journal of Climatology* **40**, 5246–5265, https://doi.org/10.1002/joc.6517 (2020).

82. Liu, Y. *et al.* Higher temperature sensitivity of retrogressive thaw slump activity in the Arctic compared to the Third Pole. *Science of the Total Environment* **914**, 170007, https://doi.org/10.1016/j.scitotenv.2024.170007 (2024).

83. *Skrifter om Svalbard og Ishavet/The place-names of Svalbard.* Vol. 80 (1942).

84. Dallmann, D. K. *Geoscience Atlas of Svalbard.* (Norsk Polarinstitutt, 2015).

85. Nicu, I. C., Rubensdotter, L., Tanyas, H. & Lombardo, L. Near Pan-Svalbard cryospheric hazards inventory (SvalCryo). *Zenodo* https://doi.org/10.5281/zenodo.10522820 (2024).

86. Sahrane, R., Bounab, A. & El Kharim, Y. Investigating the effects of landslides inventory completeness on susceptibility mapping and frequency-area distributions: Case of Taounate province, Northern Morocco. *Catena* **220**, https://doi.org/10.1016/j.catena.2022.106737 (2023).

87. Malamud, B. D., Turcotte, D. L., Guzzetti, F. & Reichenbach, P. Landslide inventories and their statistical properties. *Earth Surface Processes and Landforms* **29**, 687–711, https://doi.org/10.1002/esp.1064 (2004).

88. Tanyaş, H., Allstadt, K. E. & van Westen, C. J. An updated method for estimating landslide-event magnitude. *Earth Surface Processes and Landforms* **43**, 1836–1847, https://doi.org/10.1002/esp.4359 (2018).

89. Humlum, O., Instanes, A. & Sollid, J. L. Permafrost in Svalbard a review of research history climatic background and engineering challenges. *Polar Research* **22** (2003).

90. Harland, W. B. *The Geology of Svalbard*. 539 (The Geological Society, 1997).

91. Spolaor, A. *et al.* Climate change is rapidly deteriorating the climatic signal in Svalbard glaciers. *The Cryosphere* **18**, 307–320, https://doi.org/10.5194/tc-18-307-2024 (2024).

92. Isaksen, K. *et al.* Recent warming on Spitsbergen—Influence of atmospheric circulation and sea ice cover. *Journal of Geophysical Research: Atmospheres* **121**, https://doi.org/10.1002/2016jd025606 (2016).

93. Institute, N. P. *Svalbard Topography*, https://geodata.npolar.no/.

Acknowledgements

Author contributions

I.C.N. designed the study. I.C.N. prepared the initial dataset and wrote the draft. L.R. revised and validated the initial dataset. H.T. and L.L. developed the dataset structure and data processing methods. I.C.N., L.R., H.T. and L.L. improved the writing and structure of the final manuscript. All authors agreed to the final version of the manuscript.

Competing interests

The authors declare no competing interests.

Additional information

Correspondence and requests for materials should be addressed to I.C.N.

Reprints and permissions information is available at www.nature.com/reprints.

Publisher's note Springer Nature remains neutral with regard to jurisdictional claims in published maps and institutional affiliations.